ORIGINAL ARTICLE

Enhancing productivity and efficiency in conventional laser metal deposition process for Inconel 718 - part I: the effects of the process parameters

Simone Maffia[1] · Federico Chiappini[2] · Gianluca Maggiani[2] · Valentina Furlan[1] · Massimo Guerrini[2] · Barbara Previtali[1]

Abstract

The sustainable energy transition has spurred the development of technologies that minimize material and energy waste, such as additive manufacturing (AM). Laser metal deposition (LMD) is a promising AM technique, but its complexity and limited automation hinder its implementation in production chains. To enhance productivity, the high deposition rate LMD (HDR-LMD) technology has been developed, requiring advanced equipment and powerful laser sources. In contrast, the conventional LMD (C-LMD) process is simpler and less expensive to implement. This study aims to optimize the productivity and efficiency of C-LMD by adjusting laser power, scan speed, powder feed rate, and standoff distance on Inconel 718 single tracks. An innovative approach eliminates the need for cutting specimens to evaluate single tracks, allowing comprehensive geometric and performance characterization with limited operator involvement, making the analysis quicker and more robust. An extensive experimental campaign was conducted to examine the influence of process parameters on track geometry, productivity, and efficiency. A multi-objective optimization procedure identified parameter combinations maximizing productivity while maintaining high efficiency and desirable clad shape. The study attained deposition rates ranging from 700 to 800 g/h, with powder catchment efficiency ranging between 75 and 90%. These results were achieved using parameters including 1775 W of laser power, scan speeds ranging from 960 to 1140 mm/min, powder feed rates between 810 and 1080 g/h, and standoff distance of 9 mm. The study also clearly indicated that further potential for improving C-LMD process performance may be possible. The findings gathered in this paper are the base for the further optimization presented in the second part of the work, which is focused on multi-pass multi-layer and reaches deposition rates of 1500 g/h, promoting the implementation of C-LMD process at industrial level.

Keywords Laser metal deposition · Directed energy deposition · Productivity · Deposition rate · Efficiency · Optimization

1 Introduction

The sustainable energy transition is currently one of society's key challenges, driving the development of new solutions to reduce material and energy waste, such as the digitalization of manufacturing processes and the use of smart technologies [1]. Additive manufacturing (AM) in all of its forms is gaining popularity in a variety of industries due to its ability to significantly reduce the required and wasted material through a variety of means, ranging from stock material reduction to the realization of freeform topologically optimized components [2]. The capacity of AM to produce lightweight components is especially valuable in the aerospace industry, where weight reduction is essential [3, 4]. Furthermore, the streamlined supply chain of AM technologies is a prominent aspect in the oil and gas sector, where one-of-a-kind parts with short lead times are frequently required [5]. Due to its high deposition rate and compatibility for difficult-to-machine materials, laser metal deposition (LMD) is a viable choice for producing components made up of crucial materials such as titanium alloys and nickel-based alloys [6–10].

✉ Simone Maffia
simone.maffia@polimi.it

1 Department of Mechanical Engineering, Politecnico di Milano, Via La Masa 1, 20156 Milan, Italy

2 Nuovo Pignone Tecnologie S.r.l., Baker Hughes, Via Felice Matteucci 2, 50127 Florence, Italy

🖄 Springer

LMD is generally referred to as a productive process when compared to the other laser-based AM method, namely, laser powder bed fusion (L-PBF) [11, 12]. However, the typical deposition rate of LMD with powder is around 300–500 g/h, which is significantly higher than L-PBF but unable to meet the productivity demand of large-scale AM [13]. Recently, intense research efforts were conducted to improve the productivity of the powder LMD process, resulting in the development of the so-called high deposition rate LMD (HDR-LMD) technology. This is a variant of the conventional LMD (C-LMD) process which uses large spots of the laser ($\varnothing$ > 4 mm, up to 9 mm), high laser power p levels (p > 3000 W, up to 7500 W), and high powder feed rate pfr levels (pfr > 3000 g/h, up to 7000 g/h). The reported productivity of the process is between 2000 and 5000 g/h [14, 15]. Moving the process parameters to these extreme levels, however, necessitates the design and implementation of advanced equipment, such as nozzles and optics that can withstand the increased wear and temperature of the process, as well as very powerful laser sources. Furthermore, the majority of the examples of the application of HDR-LMD are limited to single tracks or a low number of layers [14, 16–20], and only few of them demonstrates the technology on taller structures, but with low powder catchment efficiency (~50%) [21]. Finally, it should be highlighted that the use of such a high energetic input may cause heat accumulation in the deposition, resulting in different thermal cycle effects, microstructure, and properties [15, 22, 23].

C-LMD, on the other hand, is easier and less expensive to implement in terms of machine requirements because it uses standard and well-known components. The laser spot size and power, as well as the powder feed rate, are all limited. The heat cycles of C-LMD are also less extreme than those of HDR-LMD, resulting in typically better characteristics [24, 25]. Nonetheless, with such low deposition rate performance, the technology is difficult to adapt to the deposition of massive components, as required by current industry. However, the C-LMD has yet to be tuned in terms of deposition rate and powder catchment efficiency. As a result, the quoted process performance may not reflect the full capability of the technology.

To carry out the LMD process successfully, various process parameters must be examined and adjusted, including laser power, scan speed, powder feed rate, laser spot diameter, and standoff distance, which define the deposition characteristics of the clad. Additionally, factors like hatch spacing, Z-step, and scanning strategy should be evaluated for 3D builds. Flow rate and nature of carrier and shielding gasses also play a crucial role in the build's success. Other influencing factors include machine components, optical configuration of the deposition head, nozzle, and powder particle properties [20, 26–29]. On top of this long list of process input parameters, the list of output parameters (e.g.,

deposition performance, metallurgical aspects, presence of defects, mechanical behavior) is also quite long, and it is not guaranteed that when one output is optimized, the others are in an acceptable state [30]. As a result, multi-objective optimization approaches are necessary [31–33]. However, there are no examples in literature of the contemporary optimization of productivity and efficiency for the C-LMD deposition process. Both these outputs should be considered together in order to make the process appealing to the industrial scenario for the production of large components. A high productivity is useful to reduce the production and lead times of the components, while a high efficiency helps to increase the environmental and economical sustainability of the production process [34]. However, these two performance indexes are particularly unlikely to have the same relationship with the process parameters [31, 35].

This study demonstrates that optimizing productivity (deposition rate) and efficiency (powder catchment) through a well-developed experimental procedure significantly enhances the performance of the C-LMD process. The optimization is constrained by clad shape considerations to avoid lack of fusion porosity. The extensive experimental campaign involved adjusting laser power, scan speed, powder feed rate, and standoff distance at various levels on single tracks. The evaluation of single tracks utilized an original 3D microscopy technique. Although other works proposed the use of 3D scanners or microscopes for acquiring single tracks, only few data were gathered from these, and only on few sections [33, 36]. The method proposed in this work bases the geometrical and performance evaluations on an entire volume of the track, instead of on a single section like traditional cross-sectional area analysis. This comprehensive approach collected abundant data robustly and reliably, as the algorithm elaborates the data consistently. The results from the optimization of single tracks and process characterization were then applied to manufacture thick walls with consistently high deposition rate, powder catchment efficiency, and good internal build quality. The aim is to find a proper receipt of process parameters that would increase the appeal of the C-LMD process to an industrial audience for the production of large components, as required, for example, in the oil and gas and aerospace sectors.

The work is divided into two parts. Part I describes and discusses the single track characterization method and its application in the initial investigation and optimization step. The results from this phase guide the subsequent optimization steps, mainly focusing on thick walls (multi-pass multi-layer specimens) in part II. As a result of the optimization procedure, the C-LMD process performances were significantly enhanced, achieving a deposition rate more than three times higher than the normal value for C-LMD technology, minimal wasted powder, and fully dense material. The newly established process conditions enable the
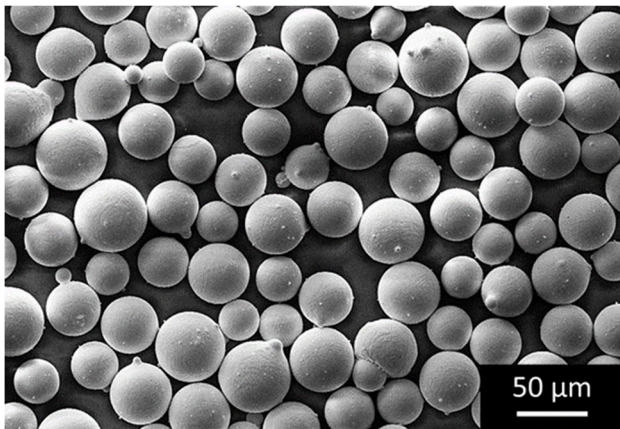
Fig. 1 SEM pictures of the employed IN718 powder

Fig. 2 Particle size distribution of the employed IN718 powder

deposition of large IN718 components in an acceptable time using a standard LMD setup.

2 Materials and methods

2.1 Powder and substrates

The entire optimization procedure described in this paper was conducted on plasma atomized Inconel 718 (IN718) alloy powder produced by AP&C—GE Additive (Saint Eustache, CA). The nominal chemical composition of the powder is compliant with the ASTM B637 (grade UNS N07718) standard [37], and the density of solid IN718 is 8.17 g/cm^3 [38]. Figure 1 depicts a SEM image of the powder, which may be used to evaluate the round shape and smooth surface of the particles, both of which are typical outcomes of the plasma atomization process. The nominal powder granulometry ranges between $d_{10} = 25$ and $d_{90} = 45$ μm, as determined by a Malvern Panalytical Ltd (Malvern, UK) Morphologi 4 optical particle size analyzer. This particle size distribution is compatible with the used LMD setup and is commonly used for metal AM processes [39, 40]. Figure 2 shows the measured particle size distribution.

AISI 304 substrates were used in the presented experimentation with a thickness of 10 mm.

2.2 C-LMD system

In this study, a CNC 5-axis LMD machine manufactured by SM Systems S.r.l. (Torre Canavese, IT) was used. The machine is equipped with three linear axes in a gantry configuration for moving the deposition head and a two-axis positioner that can rotate and tilt for handling the substrate and workpiece. The laser source is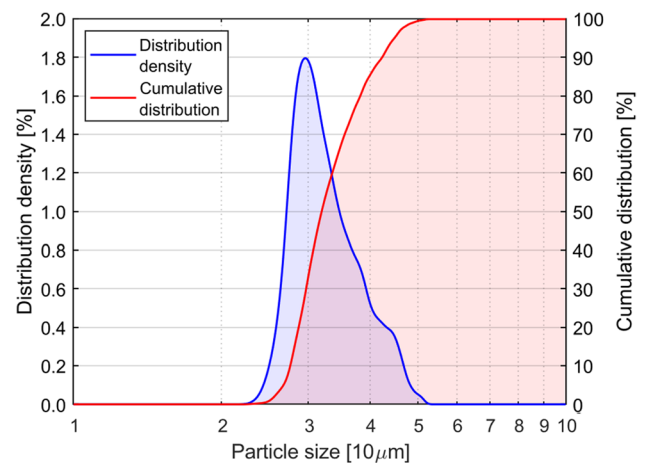 an IPG Photonics YLS-4000 (Oxford, USA) active fiber laser source, with a wavelength of 1070 nm and a maximum power of 4000 W. The laser beam is guided from the source to the deposition head by a feeding fiber and a process fiber having core diameters of 100 μm and 600 μm, respectively. These are joined by a fiber-to-fiber coupler. The deposition head is a KUKA AG MWO-I-Powder (Augsburg, DE), with a collimation lens and a focusing lens. The focal lengths of the two lenses are 129 mm and 200 mm, respectively. The laser beam emitted by the deposition head has a beam parameter product (*BPP*) of 41.8 mrad·mm. The powder feeder is a Sulzer Metco AG TWIN-10-C (Wohlen, CH), and the powder nozzle is a Fraunhofer ILT COAX-40-F (Aachen, DE). Argon was employed as a carrier gas as well as a shielding gas. Figure 3 shows an image of the interior of the LMD machine.

2.3 Single track production and characterization

In this work, the deposition of numerous single tracks is performed and consequent measurement of their geometry (width, height, contact angle, cross-section area, and volume) and deposition performance (deposition rate and powder efficiency) is required. The need for a rapid, robust, and consistent characterization approach emerged because of the high number of produced tracks and the variety of their shape. Therefore, the length of the single tracks was set at 50 mm for each experiment. Besides, a non-destructive method which does not require manual measurement of the cross-section geometry was devised. Figure 4 illustrates the developed method for determining the geometrical characteristics of single tracks.

The tracks adhered to the substrates were captured using an InfiniteFocus 3D Focus Variation optical microscope from Bruker Alicona (Graz, AT). The 2.5×
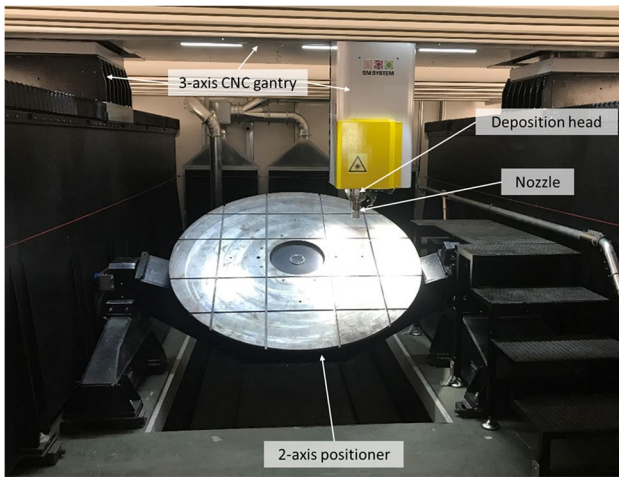
Fig. 3 The interior of the LMD machine

objective was used with a maximum resolution of 6.92 μm. A 7.5 mm long portion of the track near the end of the deposition was acquired, in the steady state part,

to reduce acquisition time and discard the first transitional phase. Furthermore, more tracks can be recorded simultaneously by utilizing the maximum mobility of the microscope stage, minimizing the required number of substrate placements (Fig. 4a). The acquisition field is rectangular on the horizontal plane. The acquisition result (Fig. 4b) is a 3D surface. Small, unmelted particles would have been captured due to the notably high spatial resolution used for the acquisitions (15 μm along x and y and 5 μm along z direction). As a result, the tracks were cleaned with a metallic brush prior to capture, ensuring that only particles that were well bonded to the track surface were of interest. Furthermore, Fig. 4b clearly shows that the substrate has an evident curvature. This is due to the substrate bending generated by residual tensions from the deposition processes. As a result, before proceeding with the extraction of the relevant geometrical aspects of the tracks, the curvature of the substrate was removed using the specific shape removal function of the Bruker Alicona MeasureSuite (Graz, AT) software.
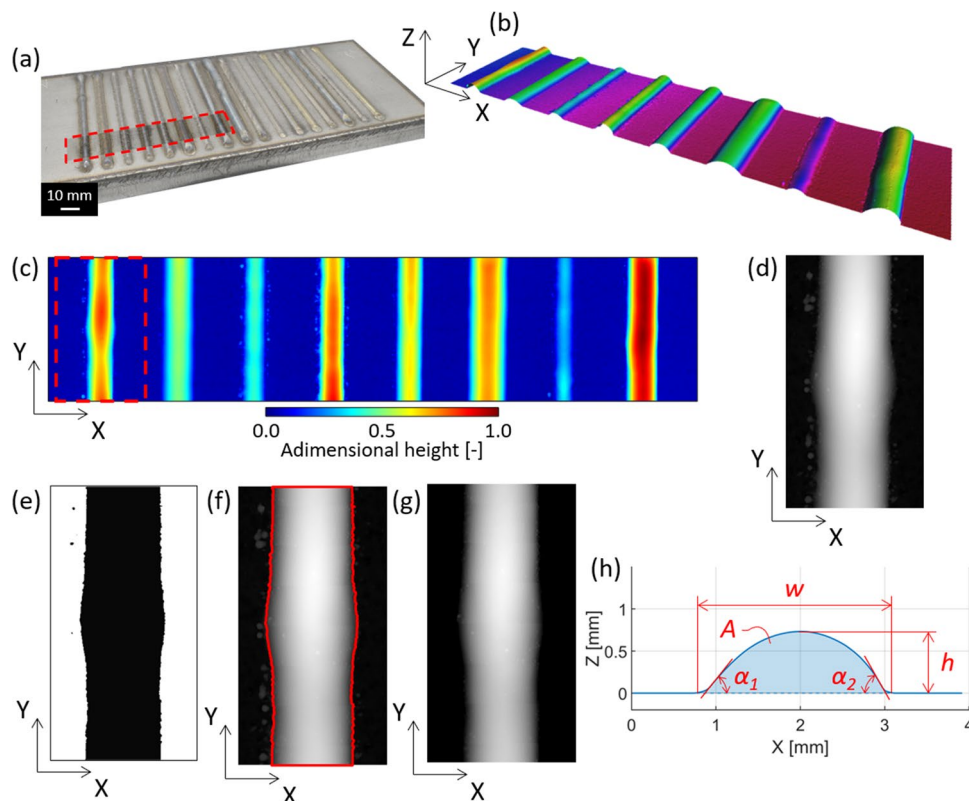

Fig. 4 Representation of the various steps of the development acquisition and elaboration method based on the 3D acquisition of the surface of single tracks: **a** the substrate plate with single tracks deposited on top of it, with an example of the acquisition field of view of the focus-variation microscope; **b** the acquired 3D surface of multiple single tracks; **c** the false color 2D picture obtained by converting the 3D scan, in which the color of a pixel represents its height; **d** a single track cut from the acquired surface and converted in monochrome scheme, where the pixel intensity level represents its height; **e** binarized picture in which the largest black blob represents the single tracks; **f** the single tracks with the detected boundary; **g** the single track rotated matching the deposition direction to the vertical direction of the image, and with the background removed; **h** the average cross-section reconstructed from the 3D volume

The rectified surface was then transformed into a point cloud file, which can be elaborated and analyzed in Matlab software, by MathWorks, Inc. (Natick, USA). The position of the points output by the microscope software is identified by a set of 3D Cartesian coordinates in the absolute reference system of the microscope and is stated in μm. Indeed, each point is identified by three values (X, Y, and Z): the first two identify the position of the point on the horizontal xy plane, while the last one indicates the height of the point from the horizontal xy plane. Therefore, the simplest method to manage this type of data is to consider the point cloud as a 2D adimensional matrix with cell values ranging from 0 (the lowest point) to 1 (the highest point). In this manner, the 3D surface can be regarded as a 2D monochrome image, with pixel intensity representing point height. Basic imaging techniques and mathematical notions can be applied on this image to identify the track and compute its 2D and 3D geometrical properties. The point cloud is transformed according to Eq. 1 to generate the 2D matrix and thus the 2D monochromatic image:

$$\begin{cases} column = \frac{X-X_{min}}{Res_H} + 1, [-] \\ row = \frac{Y-Y_{min}}{Res_H}, + 1, [-] \\ intensity = \frac{Z-Z_{min}}{Z_{max}-Z_{min}}, [-] \end{cases} \quad (1)$$

In Eq. 1, X, Y, and Z represent the 3D coordinates of a point of the point cloud; X_{min}, Y_{min}, and Z_{min} are the minimum levels reached of each coordinate; Z_{max} is the highest level of the z coordinate; Res_H is the horizontal resolution of the acquisition which is fixed at 15 μm; and *column*, *row*, and *intensity* represent the position and value of the considered cell. Figure 4c shows the result of the transformation: the 2D monochrome image is shown in pseudo-colors, with the colors representing the adimensional height of the points.

Each track in the acquisition is cropped with a rectangle from the overall picture in Fig. 4c and handled separately (Fig. 4d). To distinguish the track from the background (i.e., the substrate), hard thresholding is applied to the cropped image, with black representing the track and white representing the substrate (Fig. 4e). The selection of the appropriate threshold that separates the track from the substrate is a crucial aspect of the algorithm. Although fully-automatic methods were tested, due to the variability of the tracks, this procedure was conducted manually by the operator using an interactive GUI [41], which yielded more trustworthy and consistent results than fully-automatic methods. The deposited track is identified as the larger black blob, while the others (particles adhering to the substrate) are eliminated. Furthermore, because the track cannot be guaranteed to be perfectly aligned with the y axis, its longitudinal direction is computed as the

main axis of the ellipse with the same second moments as the larger black blob, and the image is then rotated accordingly. In Fig. 4f, the detected border is shown on top of the cropped monochromatic image. At this point, everything that is not identified as the track is set to 0, and the threshold level is subtracted from the cells corresponding to the track, so that it is placed on the 0-level surface (Fig. 4g). Finally, the average intensity of each column of the image is computed, and the adimensional values are re-translated to length values, yielding the reconstructed average cross-section of the track (Fig. 4h).

Starting from this elaboration of the scanned single track, multiple geometrical measurements can be done:

- Width, w: the average number of non-zero cells for every row of Fig. 4g
- Height, h: the average of the maximum intensity level for every row of Fig. 4g
- Contact angle, α: the average between the two angles α_1 and α_2 between the x axis and the two tangent lines of the average track profile on its two inflection points, as shown in Fig. 4h
- Volume, V_{st}: the sum of the volumes of the right truncated triangular prisms that compose the 3D track re-constructed by Fig. 4g (notice that this volume is only related to the portion of the track acquired by the microscope, and so it depends on the acquisition range in y direction)
- Cross-section area, A: the volume V_{st} divided by the number of rows of Fig. 4g

Notice that, as described in the list above, the measured would be adimensional. To convert them into dimensional values, these should be multiplied by Res_H and/or by $Z_{max} - Z_{min}$, when dealing with horizontal or vertical quantities, respectively.

Moreover, it should be noticed that the geometry of a single track is evaluated not exclusively on a single cross-section, as it is done with the standard method of cutting the track along the transversal direction, but it is averaged along a conspicuous portion of the track, yielding more significant and meaningful pieces of information. The variation of the shape of the track over its length can also be evaluated by evaluating the standard deviation of the measurement; however, this was not addressed in the current study. Furthermore, the procedure is very fast because the cross-section standard cutting procedure is eliminated, and the intervention of the operator is minimal. However, since the track can only be acquired from above, contact angles greater than 90° cannot be measured using this method due to technological limitations. In this instance, in addition to the inability to accurately determine the contact angle when greater than 90°, the track volume would also be
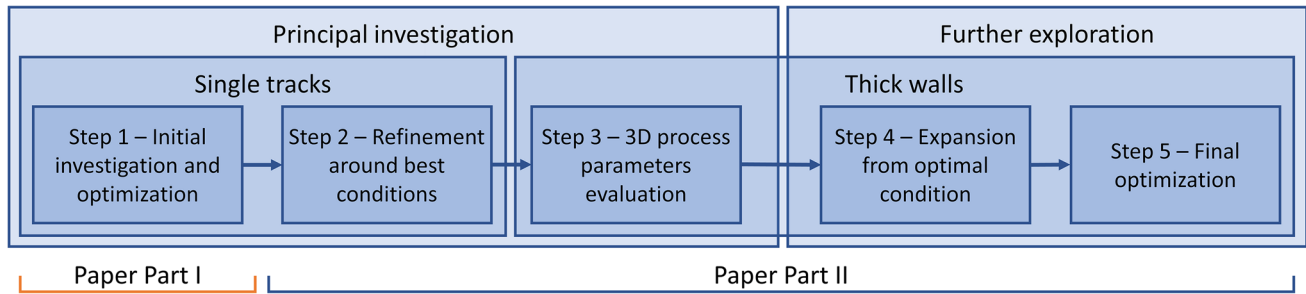
Fig. 5 A scheme of the proposed process optimization procedure. The orange bracket identifies the step covered in this part I

overstated. Despite this limitation, deposition conditions which produce a contact angle greater than 90° are not acceptable because lack of fusion issues arise, particularly in multi-pass depositions [42].

The productivity P (i.e., deposition rate) and the powder catchment efficiency E for the LMD process are defined as in Eqs. 2 and 3, respectively:

$$P = \frac{V * \rho * 60 * 60}{t * 1000}, \left[\frac{g}{h}\right] \tag{2}$$

$$E = \frac{P}{pfr} * 100, [\%] \tag{3}$$

where ρ is the material density, t is the deposition time, and pfr is the powder feed rate. In the case of single tracks geometrically measured with the abovementioned method, t can be estimated by the scan speed v and length of the acquired portion of the track l, and is referred to as t_{st}:

$$t = t_{st} = \frac{l * 60}{v}, [s] \tag{4}$$

allowing the rearrangement of Eq. 2 in:

$$P = P_{st} = \frac{V_{st} * \rho * 60}{l/v * 1000}, \left[\frac{g}{h}\right] \tag{5}$$

where P_{st} is the productivity in single tracks. The powder catchment efficiency E for single tracks can be addressed as E_{st} and derived from Eq. 2:

$$E = E_{st} = \frac{P_{st}}{pfr} * 100, [\%] \tag{6}$$

Equation 5 can be further simplified, since the volume V in single tracks (namely, V_{st}) is the product of the average cross-section area A times the length of the acquired portion of the track l:

$$V = V_{st} = A * l, \left[mm^3\right] \tag{7}$$

Finally, the productivity would be:

$$P = P_{st} = \frac{A * l * \rho * 60}{l/v * 1000} = \frac{A * v * \rho * 60}{1000}, \left[\frac{g}{h}\right] \tag{8}$$

Hence, according to Eq. 8, the productivity P_{st} is not dependent on the length of the acquired portion of the deposited track l.

3 Process optimization procedure

The proposed optimization process includes several steps, beginning with single track depositions and ending to the production of thick wall specimens. The procedure is separated into two parts: the initial campaign and its expansion. The former seeks to determine the effects of the investigated process parameters on sample geometry and, most importantly, on process performance (i.e., productivity P and powder catchment efficiency E). In addition, the primary optimization is carried out during this phase. Following that, and starting with the new optimal condition, the exploration continues to improve process performance without compromising the internal quality of the deposition. Figure 5 shows a scheme of the proposed optimization procedure.

This part I of the work only presents the initial investigation and optimization on single tracks step of the proposed optimization procedure, while part II shows the remaining steps (from 2 to 5) on both single tracks and thick walls. The experimental campaign reported in this paper lays the groundwork for all the following optimization steps, as the information gathered with this wide experimental campaign will be extensively verified and used throughout part II of the work.

3.1 Initial investigation and optimization

A non-replicated randomized full factorial experimental campaign was designed for the realization of single tracks

Table 1 Process parameters of the full-factorial experimental campaign for the initial investigation and optimization on single tracks

Fixed parameter	Level
Laser spot diameter, [mm]	2.4
Varied parameters	Levels
Laser power, p [W]	575; 875; 1175; 1475; 1775
Scan speed, v [mm/min]	420; 600; 780; 960; 1140; 1320
Powder feed rate, pfr [g/h]	270; 540; 810; 1080
Standoff distance, sod [mm]	8; 9

Table 2 Arguments used for the response optimization procedure

Response	Goal	Weight	Importance
Productivity, P_{st} [g/h]	Maximize	1	1.5
Efficiency, E_{st} [%]	Maximize	1	1
Response	Constraint		
Contact angle, α [deg]	<60		

by varying laser power p, scan speed v, powder feed rate pfr, and standoff distance sod. For these four factors, the numbers of levels were 5, 6, 4, and 2, respectively, for a total of 240 process conditions (i.e., 240 samples). All the tracks are geometrically characterized with the 3D microscopy-based method described in "Section 2.3." The analyzed outputs are the track width w, the height h, the contact angle α, the cross-section area A (as in Fig. 4f), the productivity P_{st} (Eq. 5), and the powder catchment efficiency E_{st} (Eq. 6). The process parameters are collected in Table 1.

The levels of the process parameters were chosen based on preliminary experiments, which are not reported here for brevity. These levels were selected around a standard C-LMD process condition for Inconel 718, as established in a previous study [43]. The number of levels in the plan was chosen to allow for the creation of a complete process map based on the effect of process parameters on output. A 2^k design was not appropriate for the purpose because it would have only been useful to determine the significance of the parameters to the variation of the output, not providing specific trends and not allowing to run an optimization procedure. Finally, preliminary trials were used to determine the feasibility window and the boundaries of the experimental plan, ensuring that all the conditions of the full factorial design were feasible with the setup used.

Moreover, in order to evaluate the precision and the robustness of the semi-automatic algorithm, the volume V_{st} of the smallest and of the largest single track deposit was measured ten times each. The average volume μ, the standard deviation σ, and the coefficient of variation CV, defined as the ratio of σ to μ, were calculated from the ten measurements for both clad sizes. Precision is denoted by a low CV, which means consistent measurements around the mean. Robustness is assessed by comparing CV values for the smallest and largest clads, showcasing the consistent behavior of the algorithm across different sizes.

To assess the effects of the investigated process parameters on the measured outputs, main effects plots

were generated, and ANOVAs were performed, considering second-order interactions, and fitting the data with general lineal models. Due to the large number of factors and interactions considered, the significance of the factors and their interactions was assessed using a confidence level of 0.05 corrected with the Bonferroni's approach [44]. Minitab, by Minitab, LLC (State College, USA) was used to perform a multi-objective optimization procedure using the composite desirability approach [45]. In fact, along with productivity, the powder efficiency was considered during the optimization process. This was implemented to avoid proposing solutions to the optimization procedure resulting in remarkably high productivity but with poor powder catchment efficiency, as this would compromise the sustainability of the process. Indeed, it was demonstrated that the use of recovered powder is not always possible, as parts realized with recycled powder show substantially poorer mechanical properties compared to parts produced with virgin powder [46]. Furthermore, a contact angle constraint (i.e., $\alpha < 60°$) was set to consider the internal quality of the deposition (i.e., to avoid the formation of porosities due to lack of fusion between adjacent tracks). According to the literature, the contact angle should not be greater than 80° to prevent the formation of lack of fusion pores [47]. However, for the sake of safety, 60° was chosen as the maximum value in this investigation. The arguments for the response optimization procedure are listed in Table 2.

4 Results

4.1 Initial investigation and optimization

This step of the optimization procedure required many substrates due to the large number of single tracks, which are shown in Fig. 6. A visual inspection reveals the heterogeneity of the deposited tracks.

The results of the elaboration of the acquired single tracks are shown in Fig. 7, with the detected track boundaries traced in red. Because of the number of tracks on each substrate, each substrate was acquired in two separate

Fig. 6 The single tracks of the initial investigation campaign
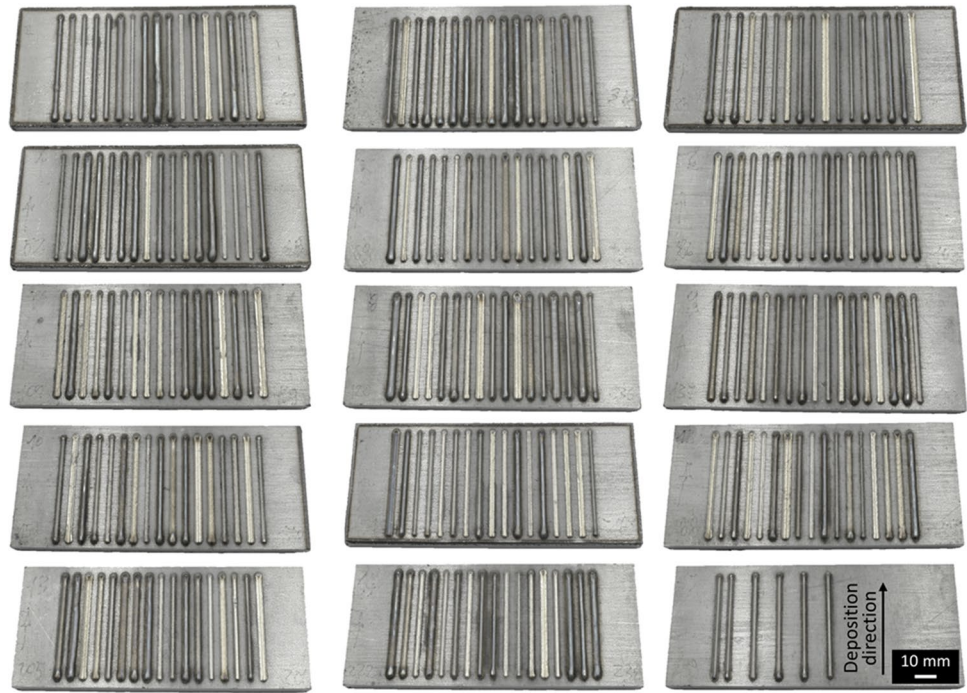
acquisitions due to the maximum field of view of the microscope. The gray level of each pixel represents the track height at that point, scaled with the maximum level of each acquisition. The reconstructed cross-sections of these tracks are depicted in Fig. 8. Only the extreme conditions of the experimental design are reported in these two figures, as if it was a 2^4 factorial campaign. Refer to the supplementary materials to see all the reconstructed cross-sections. Finally, the measurements are collected in mean effects plots (Fig. 9) and interaction plots (Fig. 10), for easier analysis of the track geometry. This type of graph can be used to conduct a qualitative evaluation of the effect of the tested process parameters. For all the 240 tested conditions, the productivity P_{st} was computed using Eq. 5, and the powder catchment efficiency E_{st} was computed with Eq. 6, directly using the measurement of the track volume.

The developed acquisition, elaboration, and characterization method based on 3D microscopy technique demonstrated the ability to detect even very small tracks. Table 3 presents the two sets of process parameters resulting in the smallest and largest clads. Furthermore, it provides the average volume μ, standard deviation σ, and coefficient of variation CV resulting from ten measurements on each track. The CV is very small (<1%) in both the considered limit process conditions, assessing the high precision and robustness of the developed measurement method.

The basic effects of the process parameters can already be assessed qualitatively in Figs. 7 and 8, but Figs. 9 and 10 allow a more clear and precise evaluation:

- The laser power p has a remarkable influence on the track width w, cross-section area A, productivity P_{st}, and efficiency E_{st}, while it has minor impact on the track height h and contact angle α.
- The scan speed v has a strong effect on all the geometrical characteristics of the tracks (width w, height h, contact angle α, and cross-section area A), but has little to no impact on the process performances in terms of productivity P_{st} and powder catchment efficiency E_{st}.
- The powder feed rate pfr provides no effect on the track width w, but it influences the track height h, contact angle α, cross-section area A, and productivity P_{st}; its effect on the efficiency E_{st} is debatable.
- The standoff distance sod has slight effects on all the observed responses.
- The interaction between scan speed v and powder feed rate pfr seems to play a role in the determination of the productivity P_{st} and of the efficiency E_{st}; other interactions may be possibly affecting the outputs, but ANOVAs are necessary to state this.

The following tables report the results of the ANOVAs of w (Table 4), h (Table 5), α (Table 6), A (Table 7), P_{st} (Table 8), and E_{st} (Table 9). The model summaries are also reported in the tables. Significant parameters and interactions are identified with an "x" in the last column of each table (the significance is assessed using a confidence level of 0.05 and the approach of Bonferroni, due to the large amount of considered factors and interactions in the model).

Fig. 7 Elaboration of single track acquisitions following the developed procedure, with the red line being the detected contour of the track (only combinations of the extrema levels of the tested process parameters are reported)
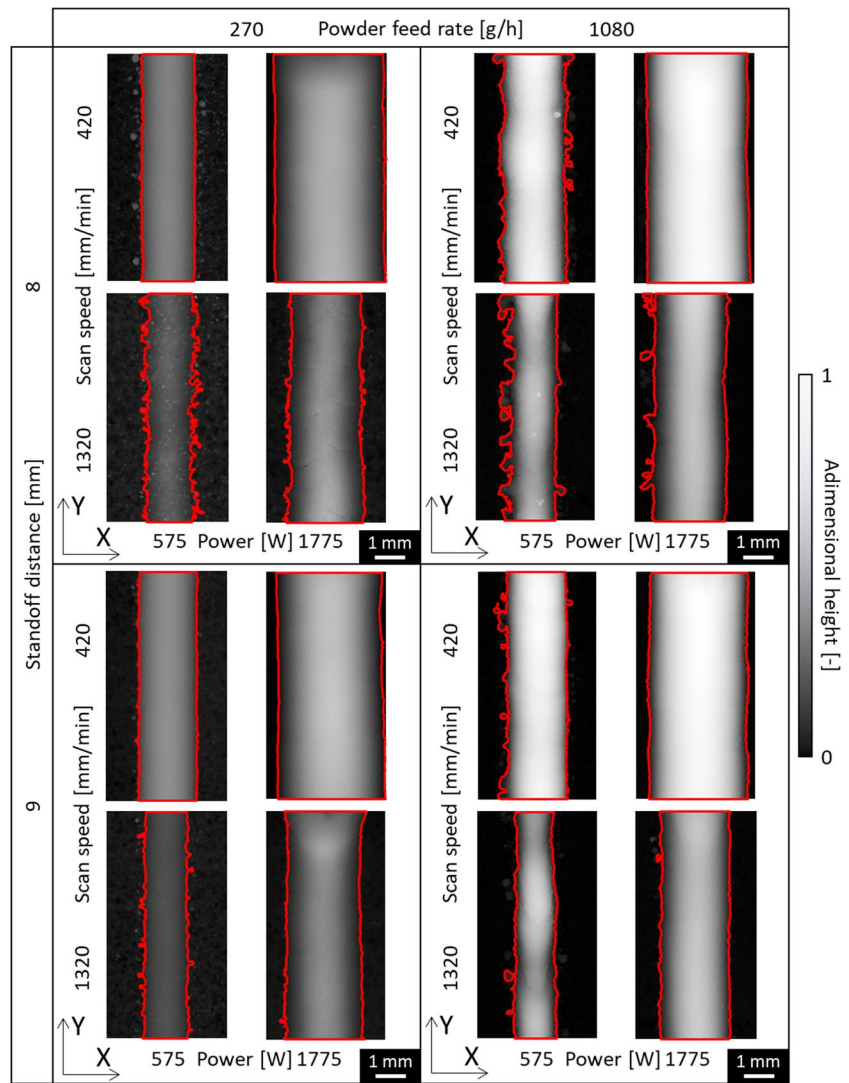
The complete general linear model was accepted for all the analyzed responses since the normality of the distribution of the standardized residuals was assessed. Furthermore, the coefficients of determination R-sq and both its adjusted R-sq(adj) and predicted R-sq(pred) variants are always remarkably high (>90%), assessing that the variance of the results is well explained by the general lineal models fitted in the ANOVAs, and that there is no overfitting. Hence, the analyses are reliable. Following the ANOVA tables, Table 10 shows the ten best solutions emerged from the optimization procedure.

The optimization through the composite desirability method states clearly that, with the given criteria, the maximum level of p should be used. In Table 10, one can roughly distinguish two sets of results: the ones with $P_{st} > 750$ g/h and $E_{st} < 80\%$, and the ones with $P_{st} < 750$ g/h and $E_{st} > 80\%$. The former category is characterized by setting the pfr at 1080 g/h (the maximum level tested for this factor), while the latter category is

characterized by setting the pfr at 810 g/h. It is difficult to detect a specific pattern in Table 10 regarding v and sod. These considerations are completely in agreement with the results of the ANOVAs and with the analysis of the main effects and interaction plots, which stated that p and pfr play remarkable roles in the determination of both P_{st} and E_{st}, while the remaining two parameters are only marginal. It should also be noted that remarkably high levels of P and E were achieved at this stage of the optimization process, and a suitable shape of the clad was maintained, despite the fact that literature typically reports 300 to 500 g/h as the common deposition rate for C-LMD of IN718 [13].

Following these considerations, it was decided to carry out the next step of the optimization procedure by considering the two best solutions proposed in Table 10. These are listed in Table 11, along with the predicted responses and their 95% confidence intervals. The continuation of the optimization procedure is reported in part II of the present work.
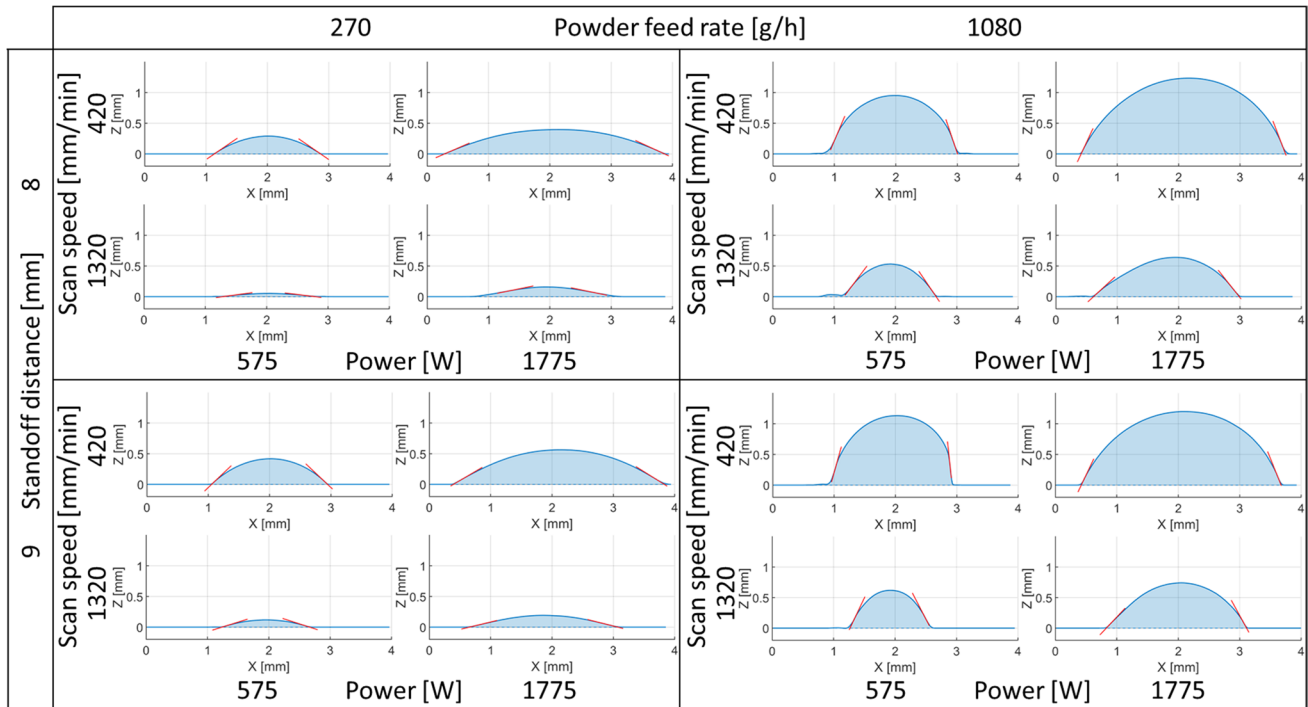
Fig. 8 Reconstruction of the cross-section of the acquired tracks obtained through the developed elaboration procedure (only combinations of the extrema levels of the tested process parameters are reported)

5 Discussion

An extensive procedural method was developed and applied in this work with the objective of optimizing productivity P and powder catchment efficiency E of the C-LMD process. The optimization should also consider the internal quality of the final multi-pass multi-layer component, which must be free from internal defects. Hence, to prevent lack of fusion due to an excessively steep contact angle, the optimization at single track level must already also take the shape of the clad into account. The method assumes that the process performance obtained in single clad depositions can be directly transferred to multi-pass multi-layer components. As a result, most of the process optimization can be done on single tracks, which are far more convenient and easier to make and handle than bulk or thick-walled specimens, allowing for the testing of many process parameters over a wide range of experimental campaigns without requiring an excessive amount of material. Indeed, in this part I of the work, only the first step of the campaign is reported. Arguably, this step is the most important part of the proposed optimization procedure, since the currently presented findings drive all the subsequent experimental campaigns shown in part II.

A novel method was developed to address the requirement for a robust and reliable comprehensive characterization of single tracks across the numerous proposed experimental campaigns, avoiding the necessity for clad cross-sections and manual measurements. The method involves using a 3D focus-variation microscope to capture the upper surface of the tracks. From there, a semi-automatic algorithm can reliably extract geometrical measurements on the deposition, such as average width w, height h, contact angle α, volume V_{st}, and cross-section area A. Based on this, the productivity P_{st} (or deposition rate) and powder catchment efficiency E_{st} can be estimated by taking the input process parameters into account. The advantage of using this method rather than the traditional one based on capturing a 2D image of the actual cross-section of the clad is that the cutting, mounting, grinding, and polishing phases are avoided, resulting in a much faster and computerized process. The operator's involvement is limited to locating the substrate in the 3D acquisition, a step crucial for accurate clad identification. Indeed, the measurements are performed automatically by the software rather than by the operator, reducing the inter- and intra-operator variability of the results. This assertion is substantiated by the analysis of the coefficient of variation CV, which reveals exceedingly minimal dispersion of values across the two extreme test conditions. This result confirms the precision and robustness of the proposed semi-automatic method. Indeed, the significantly low CV indicates remarkable consistency of measurements around the mean. Furthermore, the fact that CV remains below 1%
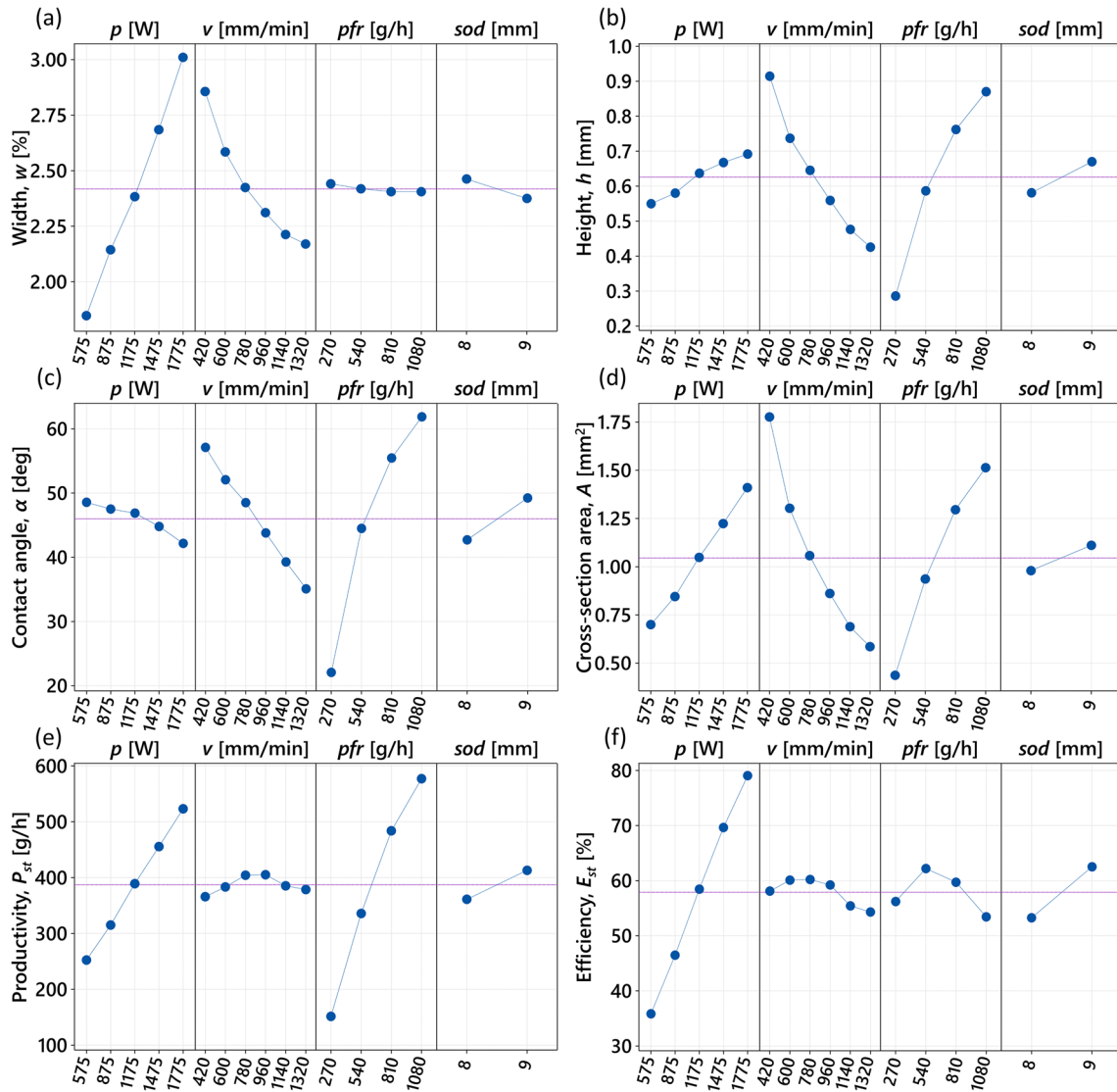
Fig. 9 Main effect plots of the measured variables on single tracks of the initial investigation and optimization campaign (pink dashed lines are the average responses): **a** track width; **b** track height; **c** contact angle; **d** cross-section area; **e** productivity; **f** powder catchment efficiency

Table 3 Process parameters and volume measurement statistics for the smallest and the largest tracks

	Smallest track	Largest track
p [W]	575	1775
v [mm/min]	1320	420
pfr [g/h]	270	1080
sod [mm]	8	9
	Volume V_{st}	Volume V_{st}
μ [mm^3]	0.387	23.438
σ [mm^3]	0.003	0.108
CV [%]	0.721	0.462

for both limit conditions highlights the robustness of the method against variations in process parameters. Since not

just a single cross-section is characterized, but an entire portion of the clad, with measurements averaged along the length of the acquired portion to improve accuracy. The method proved to be efficient, allowing the characterization of the 240 single tracks of the initial investigation and optimization step to be completed in a reasonable amount of time while yielding valuable and comparable results. The evaluation of deposition process performance (i.e., P and E) directly on single tracks is arguably a significant accomplishment of this work. Indeed, the passage through the clad volume is a fundamental aspect of the developed method. The productivity P_{st} of single track depositions could be calculated as in Eq. 8 using the cross-section area A, which is typically measured manually by the operator on a picture of a single cut cross-section. Instead, the method
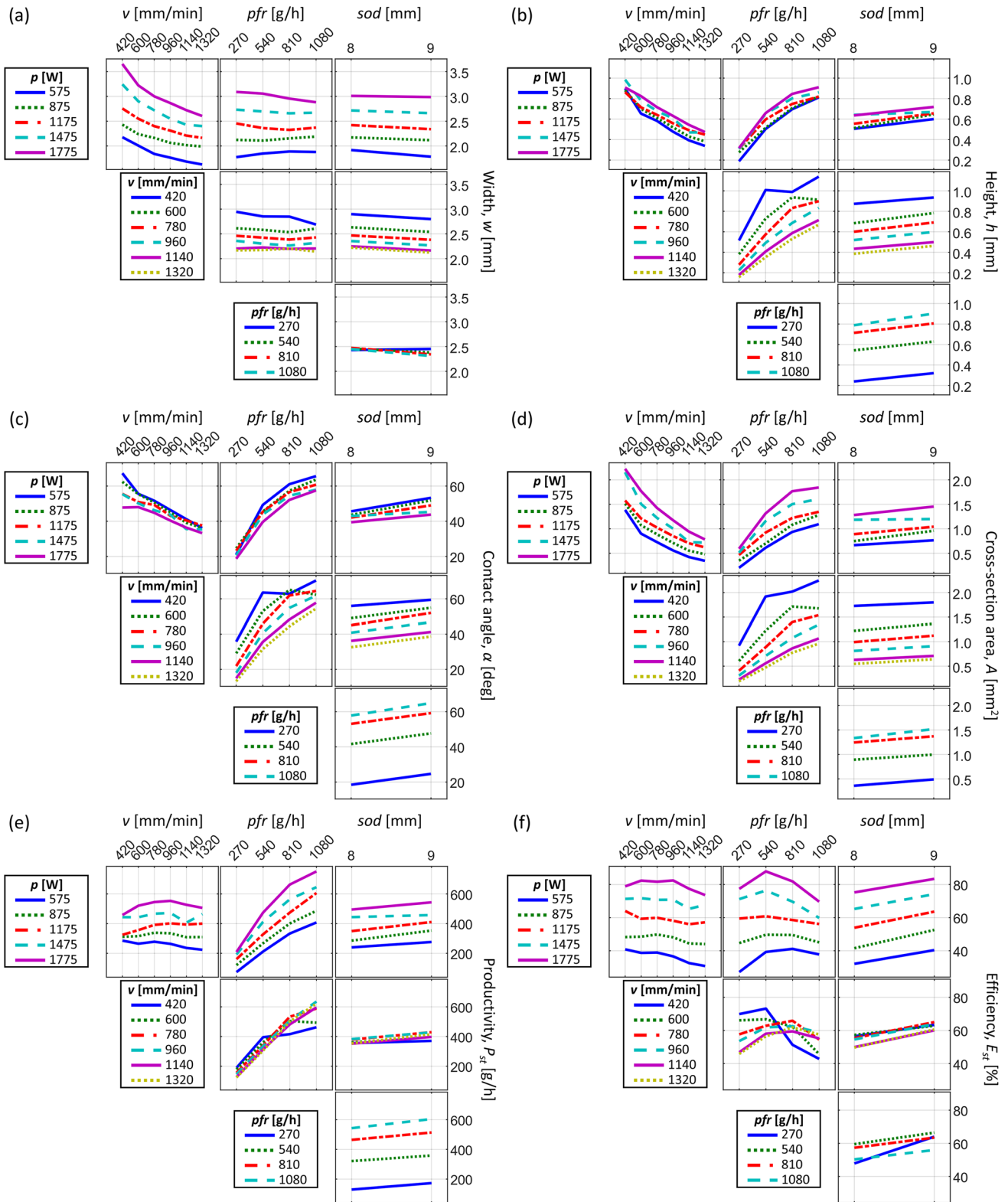
Fig. 10 Interaction plots of the measured variables on single tracks of the initial investigation and optimization campaign: **a** track width; **b** track height; **c** contact angle; **d** cross-section area; **e** productivity; **f** powder catchment efficiency

Table 4 ANOVA table for the track width of single tracks of the initial investigation and optimization campaign

Source	DF	Adj SS	Adj MS	*F* value	*P* value	Significant
Model	72	52.1535	0.72435	177.64	0.000	x
p	4	6.6755	1.66887	409.28	0.000	x
v	5	0.9719	0.19438	47.67	0.000	x
pfr	3	0.0462	0.01542	3.78	0.012	
sod	1	0.0164	0.01639	4.02	0.047	
$p*v$	20	1.2061	0.06031	14.79	0.000	x
$p*pfr$	12	0.3539	0.02949	7.23	0.000	x
$p*sod$	4	0.0565	0.01413	3.47	0.000	x
$v*pfr$	15	0.0912	0.00608	1.49	0.114	
$v*sod$	5	0.0032	0.00064	0.16	0.977	
$pfr*sod$	3	0.1708	0.05692	13.96	0.000	x
Error	159	0.6483	0.00408			
Total	231	52.8019				

Model summary

S		*R*-sq [%]		*R*-sq(adj) [%]		*R*-sq(pred) [%]
0.0638557		98.77		98.22		97.35

presented in this work directly applies Eq. 5, since the volume V_{st} of an entire portion of the track is measured. This is a significant improvement over the approximation of the single cross-section method, which assumes a constant A along the clad. This advantage is especially significant when estimating process performance, but it also applies to track geometrical characterization, which are no longer a pointwise measurement. Indeed, w, h, and α are typically measured only on a single cross-section, assuming that the track geometry is uniform along its length. Furthermore, identifying w, h, and α from a cross-section is not always a simple task, and the measurement would be significantly influenced by the operator, potentially making comparison of results difficult and unreliable. Nevertheless, the method is limited to single tracks with contact angles less than 90°. Indeed, because the tracks are reconstructed from the acquisition of their top surface, the focus-variation microscope is incapable of accurately identifying such deposition conditions, as it would underestimate α (capped at 90°) and overestimate V_{st}, as well as A, P_{st}, and E_{st}, consequently. In any case, when considering the general applications of the LMD process, deposition conditions that produce tracks with α greater (or even close to) than 90° are typically avoided (as in the current work) because they

Table 5 ANOVA table for the track height of single tracks of the initial investigation and optimization campaign

Source	DF	Adj SS	Adj MS	*F* value	*P* value	Significant
Model	72	19.3485	0.26873	147.14	0.000	x
p	4	0.0761	0.01902	10.41	0.000	x
v	5	0.3338	0.06676	36.55	0.000	x
pfr	3	1.3182	0.43939	240.58	0.000	x
sod	1	0.0566	0.05658	30.98	0.000	x
$p*v$	20	0.0394	0.00197	1.08	0.376	
$p*pfr$	12	0.0551	0.00459	2.51	0.005	x
$p*sod$	4	0.0291	0.00727	3.98	0.004	x
$v*pfr$	15	0.4828	0.03218	17.62	0.000	x
$v*sod$	5	0.0075	0.00151	0.82	0.534	
$pfr*sod$	3	0.0204	0.00680	3.72	0.013	
Error	164	0.2995	0.00183			
Total	236	19.648				

Model summary

S		*R*-sq [%]		*R*-sq(adj) [%]		*R*-sq(pred) [%]
0.0427365		98.48		97.81		96.82

Table 6 ANOVA table for the contact angle of single tracks of the initial investigation and optimization campaign

Source	DF	Adj SS	Adj MS	F value	P value	Significant
Model	72	75,357.9	1046.64	147.79	0.000	x
p	4	319.9	79.98	11.29	0.000	x
v	5	2225.5	445.09	62.85	0.000	x
pfr	3	4660.9	1553.64	219.37	0.000	x
sod	1	228.8	228.79	32.31	0.000	x
$p*v$	20	514.6	25.73	3.63	0.000	x
$p*pfr$	12	182.8	15.23	2.15	0.016	
$p*sod$	4	197.7	49.41	6.98	0.000	x
$v*pfr$	15	1982.1	132.14	18.66	0.000	x
$v*sod$	5	13.9	2.79	0.39	0.853	
$pfr*sod$	3	37.0	12.35	1.74	0.160	
Error	165	1168.6	7.08			
Total	237	76,526.5				

Model summary

S		R-sq [%]		R-sq(adj) [%]		R-sq(pred) [%]
2.66123		98.47		97.81		96.82

Table 7 ANOVA table for the cross-section area of single tracks of the initial investigation and optimization campaign

Source	DF	Adj SS	Adj MS	F value	P value	Significant
Model	72	94.4941	1.31242	195.76	0.000	x
p	4	1.8388	0.45969	68.57	0.000	x
v	5	0.4307	0.08613	12.85	0.000	x
pfr	3	4.9209	1.64032	244.66	0.000	x
sod	1	0.1129	0.11286	16.83	0.000	x
$p*v$	20	1.4173	0.07087	10.57	0.000	x
$p*pfr$	12	1.2418	0.10348	15.43	0.000	x
$p*sod$	4	0.0473	0.01183	1.76	0.139	
$v*pfr$	15	2.9980	0.19987	29.81	0.000	x
$v*sod$	5	0.0442	0.00884	1.32	0.259	
$pfr*sod$	3	0.0692	0.02306	3.44	0.018	
Error	163	1.0928	0.00670			
Total	235	95.5869				

Model summary

S		R-sq [%]		R-sq(adj) [%]		R-sq(pred) [%]
30.7949		98.86		98.35		97.58

would result in a lack of fusion porosity within adjacent tracks in multi-pass depositions [48]. Nonetheless, if the goal of the study would have been to characterize tracks with α that are willingly greater than 90°, this method could not have been used. In the current study, only three of the 240 conditions deposited for the initial investigation campaign had this characteristic, which did not mine the results of the analyses. Another limitation of this method is the inability to analyze the dilution zone of the deposition or the internal porosity of the tracks, which requires a cross-section.

The initial investigation and optimization experimental campaign is extremely broad in terms of tested factors (p, v, pfr, sod) and levels for each factor (5, 6, 4, and 2, respectively). For this campaign, 240 single tracks were deposited and characterized. Because of the high numerosity, a comprehensive and detailed characterization of the C-LMD process within the tested range of process parameters was possible, and the main effects plots in Fig. 9 and the interaction plots in Fig. 10 are very informative. These can be used not only to understand the effects of process parameters on deposition, but also as a map to predict where their variation will lead.

For example, the pfr has a significant effect on h but has no effect on w. This behavior can be explained by the energy attenuation effect due to the flying powder particles

Table 8 ANOVA table for the productivity of single tracks of the initial investigation and optimization campaign

Source	DF	Adj SS	Adj MS	F value	P value	Significant
Model	72	8,926,034	123,973	130.73	0.000	x
p	4	34,738	8685	9.16	0.000	x
v	5	48,579	9716	10.25	0.000	x
pfr	3	147,190	49,063	51.74	0.000	x
sod	1	1426	1426	1.50	0.222	
$p*v$	20	27,817	1391	1.47	0.100	
$p*pfr$	12	208,052	17,338	18.28	0.000	x
$p*sod$	4	7768	1942	2.05	0.090	
$v*pfr$	15	299,849	19,990	21.08	0.000	x
$v*sod$	5	9266	1853	1.95	0.088	
$pfr*sod$	3	3788	1263	1.33	0.266	
Error	164	155,525	948			
Total	236	9,081,559				

Model summary

S	R-sq [%]	R-sq(adj) [%]	R-sq(pred) [%]
0.0638557	98.29	97.54	96.42

Table 9 ANOVA table for the powder catchment efficiency of single tracks of the initial investigation and optimization campaign

Source	DF	Adj SS	Adj MS	F value	P value	Significant
Model	72	76,323.3	1060.05	51.03	0.000	x
p	4	6916.5	1729.13	83.24	0.000	x
v	5	3014.2	602.84	29.02	0.000	x
pfr	3	936.8	312.27	15.03	0.000	x
sod	1	640.7	640.72	30.84	0.000	x
$p*v$	20	365.6	18.28	0.88	0.613	
$p*pfr$	12	2659.8	221.65	10.67	0.000	x
$p*sod$	4	67.0	16.74	0.81	0.523	
$v*pfr$	15	7465.2	497.68	23.96	0.000	x
$v*sod$	5	362.2	72.43	3.49	0.005	x
$pfr*sod$	3	936.9	312.31	15.03	0.000	x
Error	165	3427.5	20.77			
Total	237	79,750.8				

Model summary

S	R-sq [%]	R-sq(adj) [%]	R-sq(pred) [%]
4.55770	95.70	95.70	91.07

Table 10 The ten best solutions of the optimization method for the initial investigation

Solution	p [W]	v [mm/min]	pfr [g/h]	sod [mm]	α [deg]	P_{st} [g/h]	E_{st} [%]	Composite desirability
1	1775	1140	1080	9	58.2	818	78	0.86
2	1775	960	810	9	53.6	720	90	0.86
3	1775	1320	1080	9	54.2	816	75	0.85
4	1775	1140	810	9	47.5	699	87	0.83
5	1775	960	1080	8	56.6	797	74	0.83
6	1775	780	810	8	56.1	691	84	0.81
7	1775	1320	810	9	43.5	677	84	0.80
8	1775	960	810	8	49.9	674	83	0.79
9	1775	1140	1080	8	53.7	757	70	0.79
10	1775	600	810	8	58.5	662	83	0.78

Table 11 Selected solutions of the initial investigation and optimization step with the predicted responses

	Solution 1		Solution 2	
p [W]	1775		1775	
v [mm/min]	1140		960	
pfr [g/h]	1080		810	
sod [mm]	9		9	
	Prediction	95% CI	Prediction	95% CI
w [mm]	2.62	2.55–2.69	2.75	2.68–2.82
h [mm]	0.84	0.79–0.89	0.82	0.77–0.87
α [deg]	58.2	55.3–61.1	53.6	50.7–56.5
A [mm^2]	1.51	1.42–1.60	1.56	1.47–1.65
P_{st} [g/h]	818	784–852	720	686–753
E_{st} [%]	78	73–83	90	85–95

leaving the nozzle which interact with the laser beam before reaching the substrate. These particles act like a shield and reduce the amount of energy from the laser that reaches the substrate, projecting like a shadow. A portion of the laser is reflected by the particles, and another portion of it is absorbed by the particles [49]: only the remaining part of energy is transmitted. In coaxial C-LMD, the powder cone surrounds the laser beam and converges towards its central axis. Hence, the powder particles first interact with the laser beam on the edge of the power distribution. Here the powder starts accumulating energy in the form of heat, subtracting it from the side of the energy distribution, and casting a shadow on the substrate. This subtracted thermal energy is transported to the central part of the laser track, where the powder stream converges, and this results in the increment of h [50, 51]. It was demonstrated that the shadowing (or shielding) effect increases with increasing the pfr, and for this reason h is significantly affected by pfr, while w is not [52–54]. One of the direct results of this phenomenon is that also A is increasing, which makes P_{st} increase. However, as the clad cross-section shape becomes steeper, α is also getting higher, as it may result in the formation of lack of fusion defects (also known as inter-run porosity) when depositing multi-pass structures [47, 55–60]. Indeed, when α is high, it means that there is a high amount of material at the side edges of the deposited clad. Taking into account the notable shadowing effect, indicated by the high α value, it is possible that the chosen value of p may not be sufficient to ensure proper material melting between adjacent tracks [50, 61].

Looking at the graphs, an effective way to counteract the increment of α would be to increase v, which has been shown to reduce α without affecting P_{st} or E_{st}. Indeed, increasing v shrinks the track in both directions (lateral and vertical), with a greater impact on h. As a result, A decreases, but because the time required to travel the same distance decreases as well, the quantity of material deposited per unit of time, which is P_{st}, remains nearly constant, as does the quantity of delivered material, which is indeed the pfr. When it comes to the effect of p, it causes the molten pool to expand because more energy needed to melt the delivered material is provided in the unit of time. Indeed, it is one of the most influential parameters on E_{st}, as well as on P_{st}. As a result, in order to improve process performance, p should be maximized. Although this is arguably the most important information required to improve P_{st} while maintaining a reasonable level of α (i.e., avoiding a potential source of lack of fusion porosity in multi-pass multi-layer depositions), the correct balance of the input parameters may be difficult to achieve. As a result, the multi-objective optimization method based on the composite desirability approach was used. Indeed, the output of the method (Table 10) provides a wide range of solutions to the requested optimization problem (Table 2). The findings corroborate what is shown in Fig. 9. In truth, all the proposed solutions necessitate the maximum tested level of p and one of the two maximum tested levels of pfr. On the other hand, all levels of v (except the lowest) are considered by at least one of the top ten solutions provided. As previously stated in "Section 4," two categories are proposed among these ten solutions: those with the highest pfr (1080 g/h) and those with a slightly lower pfr (810 g/h). In the former case, higher P_{st} is obtained at the expense of lower E_{st}, whereas in the latter case, the opposite is true. Considering the ten best solutions reported in Table 10, the average results are $P_{st} = 797 \pm 28$ g/h and $E_{st} = 74 \pm 3\%$ for the first category, and $P_{st} = 687 \pm 21$ g/h and $E_{st} = 85 \pm 3\%$ for the second one. Because by using the optimization parameters set in Table 2 these two categories have similar average composite desirability values (0.83 ± 0.03 and 0.81 ± 0.03, respectively), they are both recommended as valuable results. Indeed, as shown in Fig. 9e and f, maximizing pfr is beneficial to P_{st} but slightly detrimental to E_{st}. That is, the absolute amount of molten powder is increased, while the relative amount is decreased.

Although this relationship between powder catchment efficiency E and powder feed rate pfr was already observed by other research works [16, 31, 51, 59, 62, 63], there is still not a unique explanation of the phenomenon, and there is not much investigation of it [35]. A hypothesis may be based on the calorimetry law [49]. As more particles are fed into the processing zone, there is more mass absorbing the input energy. As the input energy is not accordingly increased, the overall reached temperature reduces, making the fusion of the particles and the formation of a strong bond between the clad and the substrate more difficult [64, 65]. Moreover, as the particle distribution inside the powder cone is not homogeneous [52, 66, 67], it is reasonable to suppose that a lower

fraction of them overcomes the melting temperature [68]. Unmelted powder particles reaching the molten pool on the substrate may be repelled due to the high repulsive forces generated when the solid particles interact with the liquid surface [50]. These rejected particles do not contribute to growth of the molten pool. Another explanation can be led back to the shadowing/shielding effect of the powder on the laser beam. As previously discussed, the flying particles interacting with the laser beam outside of the nozzle are reflecting and absorbing a significant portion of the delivered laser power, which is not transmitted to the substrate [49]. When the *pfr* increases, the concentration of flying particles in the powder cone increases [69]. This increases the shadowing effect, and less heat is transmitted to the substrate [53]. If a molten pool is not well formed on the substrate surface, the adhesion of the clad on it cannot occur [50]. These two explanations are most likely concurring to the reduction of powder catchment efficiency caused by an increased powder feed rate. Another factor that may influence the process performance is the powder particle size. Indeed, it is reported that also the granulometry of the blown powder influences the laser power absorption. To be more specific, employing a powder with finer particle size results in greater energy absorption by the particles as they intercept the laser beam prior to reaching the substrate. This phenomenon can potentially impact powder catchment efficiency [50, 68, 69]. However, since the same powder granulometry was consistently used in all the experimental conditions, this effect was not observed in the scope of this study.

Even though in this part I of the work only the initial investigation and optimization experimental campaign on single track is shown, the results are really promising, since good clads were deposited and very high performances were achieved. Indeed, the two best process conditions according to the optimizer (Tables 10 and 11) clearly show that deposition rate P_{st} around 700–800 g/h can be achieved by a proper analysis and tuning of the process parameters, while maintaining a high level also of powder catchment efficiency E_{st} (75–90%) and a favorable shape of the clad. Possibly, this process performance obtained at single track level could be met also in multi-pass multi-layer depositions, generalizing the results. The verification of this hypothesis is carried out in part II of the work. It should also be noticed that the performance reached in this experimental campaign is significantly higher than the generally cited as the ones of the C-LMD process, which are between 300 and 500 g/h with IN718 [13, 57].

Another consideration that is worth mentioning is that the optimizer suggests that the maximum level of p (among the tested levels) should be used to have the maximum response in terms of both P_{st} and E_{st}. Also the maximum level of *pfr*

(among the tested levels) should be chosen for this purpose, even though it is slightly detrimental to the powder catchment efficiency. This trade-off is necessary due to the differing relationships exhibited by the two outputs (P_{st} and E_{st}) with the inputs. Given the intended final application (i.e., the deposition of large components), the parameters used to run the response optimization algorithm prioritize achieving a high P_{st} over a high E_{st}. This explains why the response optimization solutions favor the maximum level of *pfr* within tested interval. However, the fact that the proposed solutions are at the border of the tested parameter ranges suggests that the experimental plan is not centered on the actual best condition of the process. Consequently, there may be room for improvement if there is the possibility to further move the process parameters, and this consideration bought to the development of the second phase (i.e., the further exploration, see Fig. 5) of the proposed optimization procedure, which is reported in part II.

6 Conclusions

In this work, a procedure for optimizing the process performance of C-LMD with powder using IN718 was designed and tested. The goal was to improve its appeal in high-demand industries like oil and gas and aerospace, where large parts need to be produced quickly, with minimal material waste and no internal defects. The optimization process began with an extensive experimental campaign on single tracks, as detailed in part I, while the subsequent steps are covered in part II.

- A novel approach for data recovery from single track depositions based on 3D surface acquisition was developed, minimizing human intervention and variability.
- Productivity and efficiency were calculated by measuring the volume of a segment of a single track, enhancing result significance.
- Extensive experimentation involved adjusting laser power, scan speed, powder feed rate, and standoff distance, with measurements of various track characteristics.
- Multi-objective optimization discovered process parameters optimizing productivity and powder catchment efficiency while addressing lack of fusion porosity in multi-pass depositions. The proposed conditions achieved productivity of 700–800 g/h and efficiency of 75–90%.

In this part I of the work, the reached levels of productivity and efficiency are already higher than what is commonly reported about the C-LMD process with IN718 [13]. Furthermore, the results suggest that further improvements may be possible by testing other sets of parameters. In part

II, the process conditions are refined and enhanced in terms of performance, finally moving to thick wall samples (i.e., multi-pass multi-layer depositions) and also to destructive controls to evaluate the material density.

Abbreviations 2D: two-dimensional; 3D: three-dimensional; AM: additive manufacturing; ANOVA: analysis of variance; C-LMD: conventional laser metal deposition; CNC: computer numerical control; CV, [%]: coefficient of variation; E, [%]: powder catchment efficiency; E_{st}, [%]: single track powder catchment efficiency; GUI: graphical user interface; h, [mm]: single track height; HDR-LMD: high deposition rate laser metal deposition; IN718: Inconel 718; l, [mm]: length of acquired portion of single track; LMD: laser metal deposition; P, [g/h]: productivity/deposition rate; p, [W]: laser power; pfr, [g/h]: powder feed rate; P_{st}, [g/h]: single track productivity/deposition rate; Res_H, [μm]: acquisition horizontal resolution; sod, [mm]: standoff distance; t, [s]: deposition time; v, [mm/min]: scan speed; V, [mm³]: deposited volume; V_{st}, [mm³]: single track volume; w, [mm]: single track width; X; Y; Z, [μm]: Cartesian absolute coordinates of the points acquired with microscope; X_{min}; Y_{min}; Z_{min}, [μm]: minimum Cartesian absolute coordinates of the point cloud; Z_{max}, [μm]: maximum Cartesian absolute vertical coordinate of the point cloud; $α$, [deg]: single track contact angle; $μ$, [mm³]: average volume; $ρ$, [g/cm³]: material density; $σ$, [mm³]: standard deviation of volume

Supplementary Information The online version contains supplementary material available at https://doi.org/10.1007/s00170-023-12196-1.

Declarations

Conflict of interest The authors declare no competing interests.

References

1. Tarancón A, Esposito V, Torrell M, Vece MD, Son JS, Norby P, Barg S, Grant PS, Vogelpoth A, Linnenbrink S, Brucki M, Schopphoven T, Gasser A, Persembe E, Koufou D, Kuhn S, Ameloot R, Hou X, Engelbrecht K et al (2022) 2022 roadmap on 3D printing for energy. J Phys Energy 4:011501. https://doi.org/10.1088/2515-7655/ac483d

2. Taddese G, Durieux S, Duc E (2020) Sustainability performance indicators for additive manufacturing: a literature review based on product life cycle studies. Int J Adv Manuf Technol 107:3109–3134. https://doi.org/10.1007/s00170-020-05249-2

3. Blakey-Milner B, Gradl P, Snedden G, Brooks M, Pitot J, Lopez E, Leary M, Berto F, du Plessis A (2021) Metal additive manufacturing in aerospace: a review. Mater Des 209:110008. https://doi.org/10.1016/j.matdes.2021.110008

4. Kittel J, Gasser A, Wissenbach K, Zhong C, Schleifenbaum JH, Palm F (2020) Case study on AM of an IN718 aircraft component using the LMD process. Procedia CIRP 94:324–329. https://doi.org/10.1016/j.procir.2020.09.061

5. Sun C, Wang Y, McMurtrey MD, Jerred ND, Liou F, Li J (2021) Additive manufacturing for energy: a review. Appl Energy 282:116041. https://doi.org/10.1016/j.apenergy.2020.116041

6. Frazier WE (2014) Metal additive manufacturing: a review. J Mater Eng Perform 23:1917–1928 10/gctr3s

7. Gradl P, Tinker DC, Park A, Mireles OR, Garcia M, Wilkerson R, Mckinney C (2022) Robust metal additive manufacturing process selection and development for aerospace components. J Mater Eng Perform. https://doi.org/10.1007/s11665-022-06850-0

8. Gibson I, Rosen D, Stucker B (2015) Directed energy deposition processes. In: Gibson I, Rosen D, Stucker B (eds) Additive manufacturing technologies: 3d printing, rapid prototyping, and direct digital manufacturing. Springer, New York, NY, pp 245–268. https://doi.org/10.1007/978-1-4939-2113-3_10

9. Murr LE, Martinez E, Amato KN, Gaytan SM, Hernandez J, Ramirez DA, Shindo PW, Medina F, Wicker RB (2012) Fabrication of metal and alloy components by additive manufacturing: examples of 3D materials science. J Mater Res Technol 1:42–54 10/f2k7wg

10. Johansson J, Persson C, Testa G, Ruggiero A, Bonora N, M. (2017) Hörnqvist Colliander, Effect of microstructure on dynamic shear localisation in alloy 718. Mech Mater 109:88–100. https://doi.org/10.1016/j.mechmat.2017.03.020

11. Moeinfar K, Khodabakhshi F, Kashani-bozorg SF, Mohammadi M, Gerlich AP (2022) A review on metallurgical aspects of laser additive manufacturing (LAM): stainless steels, nickel superalloys, and titanium alloys. J Mater Res Technol 16:1029–1068. https://doi.org/10.1016/j.jmrt.2021.12.039

12. Vafadar A, Guzzomi F, Rassau A, Hayward K (2021) Advances in metal additive manufacturing: a review of common processes, industrial applications, and current challenges. Appl Sci 11:1213. https://doi.org/10.3390/app11031213

13. Li Z, Sui S, Ma X, Tan H, Zhong C, Bi G, Clare AT, Gasser A, Chen J (2022) High deposition rate powder- and wire-based laser directed energy deposition of metallic materials: a review. Int J Mach Tools Manuf 181:103942. https://doi.org/10.1016/j.ijmachtools.2022.103942

14. Zhong C, Gasser A, Backes G, Fu J, Schleifenbaum JH (2022) Laser additive manufacturing of Inconel 718 at increased deposition rates. Mater Sci Eng A 844:143196. https://doi.org/10.1016/j.msea.2022.143196

15. Zhong C, Gasser A, Kittel J, Wissenbach K, Poprawe R (2016) Improvement of material performance of Inconel 718 formed by high deposition-rate laser metal deposition. Mater Des 98:128–134 10/ggvk7d

16. Zhong C, Biermann T, Gasser A, Poprawe R (2015) Experimental study of effects of main process parameters on porosity, track geometry, deposition rate, and powder efficiency for high deposition rate laser metal deposition. J Laser Appl 27:042003. https://doi.org/10.2351/1.4923335

17. Zhong C, Chen J, Linnenbrink S, Gasser A, Sui S, Poprawe R (2016) A comparative study of Inconel 718 formed by high deposition rate laser metal deposition with GA powder and PREP powder. Mater Des 107:386–392 10/ggvmqs

18. Zhong C, Gasser A, Kittel J, Schopphoven T, Pirch N, Fu J, Poprawe R (2015) Study of process window development for high deposition-rate laser material deposition by using mixed processing parameters. J Laser Appl 27:032008. https://doi.org/10.2351/1.4919804

19. Zhong C, Gasser A, Kittel J, Fu J, Ding Y, Poprawe R (2016) Microstructures and tensile properties of Inconel 718 formed by high deposition-rate laser metal deposition. J Laser Appl 28:022010. https://doi.org/10.2351/1.4943290

20. Zhong C, Chen J, Gasser A, Sui S, Schleifenbaum JH (2018) Microstructures, tensile properties, and fracture mechanisms of Inconel 718 formed by HDR-LMD with PREP and GA powders. Int J Adv Manuf Technol 96:2031–2041. https://doi.org/10.1007/s00170-018-1662-1

21. Li Z, Ma X, Zhong C, Sui S, Gasser A, Chen J (2022) Microstructure homogeneity and mechanical property improvement of Inconel 718 alloy fabricated by high-deposition-rate laser directed energy deposition. Mater Sci Eng A 832:142430. https://doi.org/10.1016/j.msea.2021.142430

22. Sui S, Zhong C, Chen J, Gasser A, Huang W, Schleifenbaum JH (2018) Influence of solution heat treatment on microstructure and tensile properties of Inconel 718 formed by high-deposition-rate laser metal deposition. J Alloys Compd 740:389–399 10/gc5pd8

23. Zhong C, Gasser A, Schopphoven T, Poprawe R (2015) Experimental study of porosity reduction in high deposition-rate laser material deposition. Opt Laser Technol 75:87–92 10/gjkwwh

24. Selcuk C (2011) Laser metal deposition for powder metallurgy parts. Powder Metall 54:94–99. https://doi.org/10.1179/174329011X12977874589924

25. Ma M, Wang Z, Zeng X (2015) Effect of energy input on microstructural evolution of direct laser fabricated IN718 alloy. Mater Charact 106:420–427 10/f7pzcs

26. Masaylo D, Igoshin S, Popovich A, Popovich V (2020) Effect of process parameters on defects in large scale components manufactured by direct laser deposition. Mater Today: Proc 30:665–671. https://doi.org/10.1016/j.matpr.2020.01.519

27. Sreekanth S, Ghassemali E, Hurtig K, Joshi S, Andersson J (2020) Effect of direct energy deposition process parameters on single-track deposits of alloy 718. Metals 10:96 10/ggvcsd

28. Mazzucato F, Aversa A, Doglione R, Biamino S, Valente A, Lombardi M (2019) Influence of process parameters and deposition strategy on laser metal deposition of 316L powder. Metals 9:1160. https://doi.org/10.3390/met9111160

29. Mvolo E, Sabourin L, Boisselier D (2023) An investigation of key parameters in metal additive manufacturing for robotic paths planning of large parts. Weld World 67:873–883. https://doi.org/10.1007/s40194-023-01487-6

30. Shamsaei N, Yadollahi A, Bian L, Thompson SM (2015) An overview of direct laser deposition for additive manufacturing; part II: mechanical behavior, process parameter optimization and control. Addit Manuf 8:12–35. https://doi.org/10.1016/j.addma.2015.07.002

31. Chang Y-Y, Qiu J-R, Hwang S-J (2022) Multi-objective optimization of directed energy deposition process by using Taguchi-Grey relational analysis. Int J Adv Manuf Technol 120:7547–7563. https://doi.org/10.1007/s00170-022-09210-3

32. Liang Y-J, Li J, Li A, Cheng X, Wang S, Wang H-M (2017) Experimental optimization of laser additive manufacturing process of single-crystal nickel-base superalloys by a statistical experiment design method. J Alloys Compd 697:174–181 10/f9j5c5

33. Jardon Z, Ertveldt J, Hinderdael M, Guillaume P (2021) Process parameter study for enhancement of directed energy deposition powder efficiency based on single-track geometry evaluation. J Laser Appl 33:042023. https://doi.org/10.2351/7.0000516

34. Peng T, Kellens K, Tang R, Chen C, Chen G (2018) Sustainability of additive manufacturing: an overview on its energy demand and environmental impact. Addit Manuf 21:694–704. https://doi.org/10.1016/j.addma.2018.04.022

35. Powell J, Koti D, Garmendia X, Voisey KT (2023) Assessing the quality and productivity of laser cladding and direct energy deposition: guidelines for researchers. J Laser Appl 35:012024. https://doi.org/10.2351/7.0000897

36. Mazzucato F, Forni D, Valente A, Cadoni E (2021) Laser metal deposition of Inconel 718 alloy and as-built mechanical properties compared to casting. Materials 14:437 10/gjkwwg

37. B02 Committee (2018) Specification for precipitation-hardening and cold worked nickel alloy bars, forgings, and forging stock for moderate or high temperature service, ASTM International. https://doi.org/10.1520/B0637-18

38. Wang HP, Zheng CH, Zou PF, Yang SJ, Hu L, Wei B (2018) Density determination and simulation of Inconel 718 alloy at normal and metastable liquid states. J Mater Sci Technol 34:436–439. https://doi.org/10.1016/j.jmst.2017.10.014

39. Maffia S, Furlan V, Previtali B (2023) Coaxial and synchronous monitoring of molten pool height, area, and temperature in laser metal deposition. Opt Laser Technol 163:109395. https://doi.org/10.1016/j.optlastec.2023.109395

40. Mazzarisi M, Errico V, Angelastro A, Campanelli SL (2022) Influence of standoff distance and laser defocusing distance on direct laser metal deposition of a nickel-based superalloy. Int J Adv Manuf Technol. https://doi.org/10.1007/s00170-022-08945-3

41. Image Analyst (2023). Thresholding an image (https://www.mathworks.com/matlabcentral/fileexchange/29372-thresholding-an-image), MATLAB Central File Exchange

42. Pilehrood AE, Mashhuriazar A, Baghdadi AH, Sajuri Z, Omidvar H (2021) Effect of laser metal deposition parameters on the characteristics of Stellite 6 deposited layers on precipitation-hardened stainless steel. Materials 14:5662. https://doi.org/10.3390/ma14195662

43. Maffia S, Chiappini F, Maggiani G, Furlan V, Guerrini M, Previtali B (2023) Comparison between eight-axis articulated robot and five-axis CNC gantry laser metal deposition machines for fabricating large components. Appl Sci 13:5259. https://doi.org/10.3390/app13095259

44. Bonferroni CE (1936) Teoria statistica delle classi e calcolo delle probabilità. Seeber

45. Derringer G, Suich R (1980) Simultaneous optimization of several response variables. J Qual Technol 12:214–219. https://doi.org/10.1080/00224065.1980.11980968

46. Gorji NE, O'Connor R, Brabazon D (2021) XPS, SEM, AFM, and nano-indentation characterization for powder recycling within additive manufacturing process. IOP Conf Ser: Mater Sci Eng 1182:012025. https://doi.org/10.1088/1757-899X/1182/1/012025

47. Aghili SE, Shamanian M (2019) Investigation of powder fed laser cladding of NiCr-chromium carbides single-tracks on titanium aluminide substrate. Opt Laser Technol 119:105652. https://doi.org/10.1016/j.optlastec.2019.105652

48. Ilanlou M, Shoja Razavi R, Haghighat S, Nourollahi A (2023) Multi-track laser metal deposition of Stellite6 on martensitic

stainless steel: geometry optimization and defects suppression. J Manuf Process 86:177–186. https://doi.org/10.1016/j.jmapro.2022.12.036

49. Lia F, Park J, Tressler J, Martukanitz R (2017) Partitioning of laser energy during directed energy deposition. Addit Manuf 18:31–39. https://doi.org/10.1016/j.addma.2017.08.012

50. de Oliveira U, Ocelík V, De Hosson JTM (2005) Analysis of coaxial laser cladding processing conditions. Surf Coat Technol 197:127–136. https://doi.org/10.1016/j.surfcoat.2004.06.029

51. Marzban J, Ghaseminejad P, Ahmadzadeh MH, Teimouri R (2015) Experimental investigation and statistical optimization of laser surface cladding parameters. Int J Adv Manuf Technol 76:1163–1172. https://doi.org/10.1007/s00170-014-6338-x

52. Pinkerton AJ (2007) An analytical model of beam attenuation and powder heating during coaxial laser direct metal deposition. J Phys D Appl Phys 40:7323. https://doi.org/10.1088/0022-3727/40/23/012

53. Lin J (2000) Laser attenuation of the focused powder streams in coaxial laser cladding. J Laser Appl 12:28–33. https://doi.org/10.2351/1.521910

54. Liu S, Kovacevic R (2014) Statistical analysis and optimization of processing parameters in high-power direct diode laser cladding. Int J Adv Manuf Technol 74:867–878. https://doi.org/10.1007/s00170-014-6041-y

55. dos Santos Paes LE, Pereira M, Xavier FA, Weingaertner WL, Vilarinho LO (2022) Lack of fusion mitigation in directed energy deposition with laser (DED-L) additive manufacturing through laser remelting. J Manuf Process 73:67–77. https://doi.org/10.1016/j.jmapro.2021.10.052

56. Onwubolu GC, Davim JP, Oliveira C, Cardoso A (2007) Prediction of clad angle in laser cladding by powder using response surface methodology and scatter search. Opt Laser Technol 39:1130–1134. https://doi.org/10.1016/j.optlastec.2006.09.008

57. Dalaee M, Cerrutti E, Dey I, Leinenbach C, Wegener K (2022) Parameters development for optimum deposition rate in laser DMD of stainless steel EN X3CrNiMo13-4. Lasers Manuf Mater Process 9:1–17. https://doi.org/10.1007/s40516-021-00161-3

58. Calleja A, Tabernero I, Fernández A, Celaya A, Lamikiz A, López de Lacalle LN (2014) Improvement of strategies and parameters for multi-axis laser cladding operations. Opt Lasers Eng 56:113–120. https://doi.org/10.1016/j.optlaseng.2013.12.017

59. Pellizzari M, Zhao Z, Bosetti P, Perini M (2022) Optimizing direct laser metal deposition of H13 cladding on CuBe alloy substrate. Surf Coat Technol 432:128084. https://doi.org/10.1016/j.surfcoat.2022.128084

60. Wei HL, Liu FQ, Liao WH, Liu TT (2020) Prediction of spatiotemporal variations of deposit profiles and inter-track voids during laser directed energy deposition. Addit Manuf 34:101219. https://doi.org/10.1016/j.addma.2020.101219

61. Zhou C, Zhao S, Wang Y, Liu F, Gao W, Lin X (2015) Mitigation of pores generation at overlapping zone during laser cladding. J Mater Process Technol 216:369–374. https://doi.org/10.1016/j.jmatprotec.2014.09.025

62. Donadello S, Furlan V, Demir AG, Previtali B (2022) Interplay between powder catchment efficiency and layer height in self-stabilized laser metal deposition. Opt Lasers Eng 149:106817. https://doi.org/10.1016/j.optlaseng.2021.106817

63. Sohrabpoor H (2016) Analysis of laser powder deposition parameters: ANFIS modeling and ICA optimization. Optik 127:4031–4038. https://doi.org/10.1016/j.ijleo.2016.01.070

64. Toyserkani E, Khajepour A, Corbin S (2003) Three-dimensional finite element modeling of laser cladding by powder injection: effects of powder feedrate and travel speed on the process. J Laser Appl 15:153–160. https://doi.org/10.2351/1.1585087

65. Maffia S, Furlan V, Previtali B (2023) Molten pool temperature monitoring in laser metal deposition: comparison between single wavelength and ratio pyrometry techniques. International Journal of Mechatronics and Manufacturing Systems 16:96–111. https://doi.org/10.1504/IJMMS.2023.132027

66. Lin J, Hwang B-C (1999) Coaxial laser cladding on an inclined substrate. Opt Laser Technol 31:571–578. https://doi.org/10.1016/S0030-3992(99)00116-4

67. Pinkerton AJ, Li L (2004) Modelling powder concentration distribution from a coaxial deposition nozzle for laser-based rapid tooling. J Manuf Sci Eng 126:33–41. https://doi.org/10.1115/1.1643748

68. Tabernero I, Lamikiz A, Martínez S, Ukar E, López de Lacalle LN (2012) Modelling of energy attenuation due to powder flow-laser beam interaction during laser cladding process. J Mater Process Technol 212:516–522 10/b8b2tn

69. Liu J, Li L, Zhang Y, Xie X (2005) Attenuation of laser power of a focused Gaussian beam during interaction between a laser and powder in coaxial laser cladding. J Phys D Appl Phys 38:1546. https://doi.org/10.1088/0022-3727/38/10/008

Publisher's note Springer Nature remains neutral with regard to jurisdictional claims in published maps and institutional affiliations.